In vivo CRISPR screening identifies regulators of hyperplastic and hypertrophic adipose remodelling in zebrafish

Rebecca Wafer*, Panna Tandon* and James E. N. Minchin#

Centre for Cardiovascular Science, College of Medicine and Veterinary Medicine, University of Edinburgh, Scotland, United Kingdom

* Indicates equal contributions. # indicates author for correspondence: james.minchin@ed.ac.uk

Abstract

Adipose tissues exhibit a remarkable capacity to expand, regress, and remodel in response to energy status. The cellular mechanisms underlying adipose remodelling are central to metabolic health. Hypertrophic remodelling - characterised by the enlargement of existing adipocytes - is associated with insulin resistance, type 2 diabetes, and cardiovascular disease. In contrast, hyperplastic remodelling – in which new adipocytes are generated - is linked to improved metabolic outcomes. Despite its clinical importance, the regulation of hypertrophic and hyperplastic adipose remodelling remains poorly understood. In this study, we first leveraged human genetic and transcriptomic data to identify candidate genes involved in adipose remodelling. We then developed a quantitative imaging pipeline to assess hyperplastic and hypertrophic morphology in zebrafish subcutaneous adipose tissue, and applied it in an F0 CRISPR mutagenesis screen targeting 25 candidate genes. This screen identified six genes that significantly altered adipose morphology; including Sushi Repeat Containing Protein (Srpx) - a gene with previously unknown roles in adipose. Among the identified genes, *foxp1b* mutants were notable for inducing hypertrophic morphology. To investigate further, we generated stable loss-of-function alleles for both zebrafish *foxp1* genes. We found that *foxp1b* mutants display a developmental bias towards hypertrophic adipose growth but fail to undergo further hypertrophic remodelling in response to a high-fat diet - suggesting that early developmental patterning constrains later adaptability to diet. Together, these findings establish a scalable and tractable in vivo screening platform for identifying regulators of adipose remodelling, and reveal a potential developmental influence on the capacity for diet-induced adipose expansion.

Introduction

Adipose tissues exhibit a remarkable capacity to remodel and restructure themselves in response to the energetic status, the environment, physiological demands, or disease. Adipose remodelling involves alterations in both adipocyte number (addition or removal of adipocytes) and adipocyte size (expansion or reduction in adipocyte size). Increases in adipocyte size (hypertrophy) can trigger hypoxia, necrosis, altered lipid flux, inflammation and insulin resistance (1–3). Accordingly, a hypertrophic adipose morphology – adipose characterised by few, large adipocytes – is associated with increased cardiometabolic disease (4–6). Contrastingly, a hyperplastic adipose morphology - characterised by many, small adipocytes - is associated with more metabolically beneficial outcomes (7,8). Indeed, reductions in the hyperplastic potential of mouse adipose is associated with decreased insulin sensitivity (9), and disruption of adipocyte progenitor differentiation, proliferation and renewal leads to adipose hypertrophy and ensuing metabolic dysfunction (10). Strikingly, adipose hypertrophy is increased and preadipocyte frequency is reduced in diabetic obese patients (relative to non-diabetic obese) (11), and genetic predisposition for Type 2 diabetes, but not obesity, is

associated with an impaired ability to recruit new adipose cells to store excess lipids in the subcutaneous adipose tissue (12). Despite its clinical relevance, the genetic, cell and molecular processes that determine the capacity for hyperplastic and/or hypertrophic adipose plasticity are largely unknown but will be key for treating and understanding adipose-related disease.

The zebrafish provides a tractable and powerful in vivo model for studying adipose growth and remodelling dynamics. Zebrafish adipose tissue is morphologically similar to mammalian white adipose tissue, comprising large adipocytes with a single dominant cytoplasmic lipid droplet (13,14). Transcriptomic profiling further supports this conservation, with RNA-Seq data revealing strong molecular similarity between zebrafish and mammalian white adipose tissue (15). Functionally, zebrafish adipose depots respond dynamically to nutritional status - expanding following a high-fat diet and regressing following food restriction (16,17). Further, prolonged high-fat or overfeeding has been shown to induce diabetic phenotypes in zebrafish (18,19), reinforcing the model's relevance to metabolic disease. One of the key advantages of the zebrafish model is its optical accessibility and amenability to fluorescent imaging. Lipophilic dyes such as Nile Red can be used to label lipid droplets (LDs) in vivo (13,20), and LD-associated protein reporters now allow real-time visualisation of lipid droplet dynamics in living animals enabling rapid assessment of adiposity and LD morphology (21,22). Additionally, transgenic tools are increasingly available to label and manipulate zebrafish adipocytes (23,24). Importantly, zebrafish are amenable to targeted CRISPR screens, and recent studies have utilised this methodology to examine roles for candidate obesity genes (25,26). However, to date, the zebrafish model has not been applied to systematically study the cellular growth properties of adipose tissue—specifically the regulation of hyperplastic versus hypertrophic remodelling.

Here, we leverage transcriptomic data from human subcutaneous adipose to identify genes associated with hyperplastic/hypertrophic adipose morphology. We then establish an image-based method for quantifying hyperplastic/hypertrophic morphology signatures in zebrafish, and apply it in a CRISPR screen targeting 25 candidate morphology genes. We identify six genes that alter adipose morphology, three whose disruption induces hypertrophic morphology (*foxp1b*, *txnipa* and *mmp14b*), and three that induce hyperplastic morphology (*ptenb*, *cxcl14* and *srpx*). To our knowledge, one of these - Sushi Repeat Containing Protein (Srpx) – has no previously characterised

78 roles in adipose biology. For functional follow-up, we focus on Foxp1, a transcription factor known to
79 regulate stem and progenitor cells maintenance across multiple tissues. We generated new stable
80 mutant lines for the two zebrafish *foxp1* genes (*foxp1a* and *foxp1b*), and find that mutation of *foxp1b*
81 leads to a developmental bias towards hypertrophic growth, but an inability to undergo hypertrophic
82 growth in response to high-fat diet. These findings suggest that early developmental patterning of
83 adipose morphology may influence subsequent capacity to respond to diet-induced remodelling.

84

85 Methods

86 Identification of differentially expressed genes associated with small or large adipocytes in 87 human subcutaneous adipose

88 Differentially expressed genes (DEGs) associated with large or small adipocytes in human SAT were
89 obtained from Honecker et al., 2022. Briefly, 3,727 genes were significantly associated with adipocyte
90 area by both categorical and continuous statistical models (FDR < 0.05) (27). 2,190 DEGs were
91 associated with small adipocyte area, 1,537 DEGs associated with large adipocyte area (**Suppl. Table
92 1**). Expression within human WAT cell types for each of the candidate morphology genes was
93 determined using data from (28) via the Single Cell Portal
94 (https://singlecell.broadinstitute.org/single_cell). Scaled mean expression for each of the
95 morphology DEGs was assessed within each of the 16 previously defined WAT cell clusters (adipose
96 stem and progenitor cells (ASPCs), mesothelium, pericyte, adipocyte, macrophage, endothelial, LEC,
97 monocyte, T cells, dendritic cells, smooth muscle cells, b cells, mast cells, natural killer cells,
98 endometrium, and neutrophils). Of the 3,727 morphology genes, the following were removed: 410
99 genes without annotations in bulk RNA-Seq dataset, 250 genes not found in the Single Cell Portal
100 dataset, and 87 genes not expressed in the 16 WAT cell types. Hierarchical clustering of the remaining
101 2,980 morphology genes based on WAT cell type expression was performed in Morpheus
102 (https://software.broadinstitute.org/morpheus) using an average linkage method and one minus
103 Pearson correlation metric (**Suppl. Fig. 1**). Morphology genes enriched in ASPCs were identified as
104 either (i) belonging to the 75 morphology DEGs within the ASPC cluster, or (ii) one of the top 50
105 morphology DEGs with highest scaled mean expression in ASPCs (**Suppl. Table 2**). Three genes were
106 present in both categories (*CXCL14*, *KAZN* and *SPARC*), resulting in 122 ASPC-enriched morphology

107 DEGs (**Suppl. Table 2**). Ribosomal genes were excluded along with genes that did not code for
108 proteins, resulting in 102 candidate morphology genes (**Suppl. Table 2**).

109

110 Prioritisation and ranking of candidate adipose morphology genes

111 Enrichment analysis on the 102 candidate genes described above was performed using GProfiler
112 (https://biit.cs.ut.ee/gprofiler/gost), with the 3,727 original genes as a background gene set. Six
113 enriched GO biological process gene sets were identified, comprising; three 'developmental' terms
114 (GO:0048869, GO:0009888 & GO:0032502), one 'differentiation' term (GO:0030154), and two more
115 generic 'process' terms (GO:0048869 & GO:0048523) (**Suppl. Table 3**). For each of the 102
116 morphology genes, beta coefficients between SAT expression levels and the 23 cardiometabolic traits
117 from the METSIM study were clustered in Heatmapper (www.heatmapper.ca) using an average
118 linkage clustering method and Pearson distance measurement method (**Suppl. Fig. 2**). Correlations
119 between SAT expression and 23 cardiometabolic traits from 770 males as part of the METSIM study
120 were obtained from (29). The following genes were not found in the METSIM data: *EIF4EBP3*, *PDF*,
121 *SELENOM* and *SELENOS*. Candidate body mass index (BMI) and waist-to-hip ratio (WHR) genome-
122 wide association study (GWAS) genes were identified by (i) downloading summary statistics for BMI
123 and WHR from the GWAS Catalog (https://www.ebi.ac.uk/gwas/), (ii) identifying unique variants
124 associated with the traits at genome-wide significance ($p < 5 \times 10\text{-}8$), (iii) calculating proxy variants in
125 in high linkage disequilibrium in CEU population (R2>0.8), (iv) calculating 'LD blocks' that encompass
126 each lead and associated proxy variants and (v) identifying genes that overlap with the LD blocks. The
127 DIOPT Ortholog Finder (https://www.flyrnai.org/cgi-bin/DRSC_orthologs.pl) was used to identify
128 zebrafish orthologs of the candidate human morphology genes based on the weighted score. The
129 'alignment & scores' function in DIOPT was used to calculate protein similarity between human and
130 zebrafish genes. scRNA-Seq scaled mean expression and % of cells expressing candidate genes from
131 Yang Loureiro et al. (2023) were obtained from the Single Cell Portal.

132

133 Zebrafish husbandry and maintenance

134 Zebrafish were housed in the Queen's Medical Research Institute (QMRI) facility at the University of
135 Edinburgh, UK. Standard husbandry was followed on a recirculating system and a 14h:10h light to

136 dark cycle. Feeding regimen was as described in Tandon et al., 2025. The wild-type line used were
137 WIKs maintained at the QMRI facility. Zebrafish experiments were conducted in accordance with the
138 UK Animals (Scientific Procedures) Act 1986 under the project licence PP9112175.

139

140 F0 CRISPR screen in zebrafish

141 We followed general CRISPR screen methodology (30–32). Between three and five guide RNAs
142 (gRNAs) were designed to target each gene using the UCSC Genome browser track
143 ZebrafishGenomics (31) and CHOPCHOP software. gRNAs were selected based on off-target and
144 efficiency scores, along with location in gene (targeting early exons, functional domains, and avoiding
145 exons with lengths divisible by three). Pooled in vitro transcription of gRNAs was performed as per
146 Wu et al (2018), and RNA was cleaned using Zymoclean columns (Zymo Research, Cat. # R1013). Prior
147 to injection, gRNAs were incubated with Cas9 protein (New England Biolabs, Cat. # M0646T) and
148 heated for 5 mins at 37°C. Mutagenesis of individual gRNAs was verified using T7E1 assays (New
149 England Biolabs, Cat. # M0302S). gRNAs were injected into zebrafish embryos at the one-cell stage
150 as per Wu et al 2018, along with a Fast Green dye to screen for successfully injected embryos.
151 Identical injection mixes lacking the gRNAs (Cas9-only control) were used for control groups. 50
152 injected embryos were placed per petri dish and screened for survival at 5 days post fertilisation
153 (dpf). At 5 dpf, injected larvae were placed in a small volume of system water in a 1L nursery tank
154 without running water. From 10 dpf, a slow flow of system water was introduced. Larvae were raised
155 at a density of 25 per 1L nursery tank, before being transferred to a 3L tank at 21 dpf. Survival was
156 further assessed at 21 dpf. Feeding regimen was as described for standard husbandry. At 36-42 dpf,
157 fish were euthanised and Nile Red staining performed as described previously (16).

158

159 Image-based adipose morphology profiling in zebrafish

160 For each Nile Red-stained juvenile zebrafish, we took two images on a Leica M205 FCA fluorescence
161 stereomicroscope with a 1x objective: a whole animal image to allow use to measure total adiposity
162 and standard length (SL), and a higher magnification image of the lateral subcutaneous adipose tissue
163 (LSAT) along the zebrafish flank (hereafter referred to just as subcutaneous adipose or SAT). Images
164 were always taken of the right side of the fish, as zebrafish adipose shows left-right asymmetry, with

165 the right side containing the majority of pancreatic adipose. Images were first processed in
166 Fiji/ImageJ and the 'Clear Outside' function was used to reduce image size and focus on the SAT area
167 of interest or wider zebrafish. LD SAT images were then imported to Cellpose v2.2 and segmented
168 using the 'cyto' model (33). Automated segmentations were assessed and manually adjusted to
169 correct errors. Segmented masks and object outlines were imported to Fiji/ImageJ where xy
170 coordinates for each segmented LD along with LD measurements were taken (including Feret's
171 diameter for LD size). ImageJ macros used for the importation of Cellpose masks and measurement
172 of xy coordinates are available at github.com/jeminchin/morphology_screen. Total adipose area and
173 SAT area were segmented using Ilastik software as previously described (34). Standard length was
174 measured using the line tool in Fiji/ImageJ.

175

176 Statistical analysis of morphology values for the zebrafish F0 CRISPR screen

177 To calculate hyperplastic/hypertrophic adipose morphology we followed methodology from (35),
178 and used an initial dataset of 194 Nile Red-stained wild-type zebrafish to fit a generalised additive
179 model (GAM) to capture the relationship between SAT area and mean SAT LD diameter. Morphology
180 value was calculated as the deviation of individual mean LD diameters from the fitted model. To
181 compare hyperplastic/hypertrophic adipose morphologies between control and CRISPR mutants, we
182 first trained a GAM from either (i) experiment-specific control data (eg, Cas9-only injected controls),
183 or (ii) control data pooled from multiple experiments (n = 343 control zebrafish). These trained
184 models were then applied to mutant test data to assess morphology values (i.e. mean mutant LD
185 diameter deviation from the training model) using the mgcv package in R. To assess differences in
186 morphology values between CRISPR mutants and controls, we conducted Kolmogorov–Smirnov (KS)
187 tests to assess overall distribution shape differences. P values were corrected for multiple tests using
188 Benjamini-Hochberg FDR correction (23 tests performed, adjusted p value < 0.05). We performed KS
189 tests using both experiment-specific and pooled control data. Secondly, to complement the KS tests,
190 we log-transformed SAT area and mean SAT LD diameter to linearise the relationship and performed
191 linear mixed-model regression with replicate as a random effect to control for replicate-specific
192 effects. Using this method, we assessed both intercept and slope differences between CRISPR mutant
193 (pooled replicates) and experiment-specific controls or pooled controls. P values were corrected for
194 multiple tests using Benjamini-Hochberg.

195

196 ## Generation of *foxp1a* and *foxp1b* mutant zebrafish lines

197 *foxp1a* and *foxp1b* zebrafish mutant lines were made using standard CRISPR-Cas9 methods (34). For
198 both genes we targeted the highly conserved DNA-binding Forkhead domain (FHD). The location and
199 sequence of the CRISPR gRNAs were: *foxp1a* – 5'-GACGAGTGGAGAATGTGAAG-3' targeting the FHD
200 in exon 14, and *foxp1b* – 5'-GATAACGAAGCATACGTGAA-3' targeting the FHD in exon 15. We
201 generated two alleles - ed116 is a 13bp indel in the forkhead domain of *foxp1a* resulting in a
202 frameshift and premature stop codon, and ed125 is a 4bp indel in the forkhead domain of *foxp1b*
203 resulting in a frameshift and premature stop. Primers to amplify locus surrounding lesions for T7E1
204 assays or sequencing were: ed116 forward – 5'-GCCAGATTGGACTGGATGTT-3', ed116 reverse – 5'-
205 TTATTTCCAGGCCATTCTGG-3', ed125 forward – 5'-TTCAGTTTCAGCTCCTTCCTTC-3', ed125 reverse –
206 5'-TGGAAGTCAAGCTACCAGCA-3'. To genotype ed116, primers were designed to recognise wither
207 the 13bp indel or the wild-type sequence. Sequences were: forward – 5'-GCCAGATTGGACTGGATGTT-
208 3', reverse - 5'-TTATTTCCAGGCCATTCTGG-3', wild-type – 5'-ACGAGTGGAGAATGTGAAGG-3', ed116
209 – 5'-AAACGGCCCCCTCGTACT-3'. For ed125, the following primers were used to amplify the locus:
210 forward – 5'-TTCAGTTTCAGCTCCTTCCTTC-3', and reverse – 5'-TGGAAGTCAAGCTACCAGCA-3'. The
211 PCR product was then digested with the restriction enzyme HpyCH4IV (New England Biolabs, Cat. #
212 R0619S). Additionally, KASP genotyping assays were designed for the ed116 and ed125 alleles (KASP
213 on demand, LGC Biosearch Technologies). Western blots were performed to assess effect of
214 mutations on Foxp1 protein. Protein was isolated from the caudal fin - a pool of seven fin samples
215 was placed on dry ice in RIPA buffer (Thermo, Cat. # 8990) containing protease inhibitor (Thermo,
216 Cat. # A32953). Samples were homogenised with a TissueRupter, centrifuged for 15 mins at 4C, lysate
217 removed and added to LDS blue (Novex, Cat. # B0008) with reducing agent (Novex, B0009), heated
218 to 95C for 10 mins and the centrifuged for 1 min. Protein samples were run on 8% Bis-Tris gels
219 (Invitrogen, NW00082BOX) and run together with protein ladder (Thermo Scientific, Cat. # 26619).
220 Foxp1 antibody was PA5-26848 (Thermo Fisher) and b-actin antibody was (Sigma, A2228). Blood
221 assays were from Biovision (Glucose – K606-100, triacylglyceride – K622-100, cholesterol – K623-100)
222 and performed as per the manufacturer's instructions with 1 ul of blood from an adult zebrafish used
223 for the glucose and cholesterol assays, and 0.2 ul for the triacyclglyceride assay. qRT-PCR was
224 performed on a Roche LightCycler 480 using Luna reagents (New England Biolabs, Cat. # M3003L).
225 cDNA was synthesised using Superscript IV (Invitrogen, Cat. # 18090010). Primers were: *foxp1a*

226 forward 5'-GGCCACTTTGAGGATGACTC-3', *foxp1a* reverse 5'-CCTCGCCACCTAAAACTCAG-3', *foxp1b*
227 forward 5'-CATTGGCTCCTCTTTTACGC-3', *foxp1b* reverse 5'-ACAGCAACGGTAGTGACAGC-3', *bactin*
228 forward 5'-GCCTCCGATCCAGACAGAGT-3' and *bactin* reverse 5'-TGACAGGATGCAGAAGGAGA-3'.

229

230 ### High-fat diet in zebrafish

231 A high-fat immersion diet was conducted on juvenile fish at 35 dpf. Genotyped fish were stained with
232 Nile Red, imaged on a Leica M205 FCA stereoscope and recovered individually in a 12-well plate
233 whilst the SL of each fish was measured. Based on SL, fish were placed into groups with equal average
234 SL. Within groups, fish were randomly paired up and placed two fish per mesh insert in a 10L tank on
235 the recirculating system, allowing pairs of fish to be tracked through the experiment. The location of
236 each pair was randomly rotated daily to minimise tank location-effects. Fish assigned to the high-fat
237 diet group were immersed in 5% chicken egg yolk for two hours daily over the course of 14 days (16).
238 Control fish were placed in fresh system water for two hours daily. Both control and high-fat groups
239 received an additional two feeds throughout the day.

240

241 ### Code availability

242 All code used in this manuscript are available at github.com/jeminchin/morphology_screen.

243

244 ## Results

245 ### Identification of 102 candidate human adipose morphology genes enriched in adipocyte
246 stem and progenitor cells

247 To identify candidate regulators of hyperplastic/hypertrophic adipose morphology, we leveraged
248 previously published bulk RNA-Seq data that reported 3,727 differentially expressed genes (DEGs) in
249 human subcutaneous adipose tissue (SAT) characterised by either large or small adipocytes (**Fig. 1;**
250 **Suppl. Table 1**) (27). We reasoned these DEGs may contribute to establishing hypertrophic or
251 hyperplastic adipose phenotypes. As the RNA-Seq was performed on whole SAT - comprising a
252 heterogeneous mix of cell types - we next asked which adipose-resident cell populations

253 preferentially express these morphology-associated genes. To address this, we clustered the 3,727
254 candidate genes based on their relative expression across 16 human white adipose tissue (WAT) cell
255 types, using published single-cell transcriptomic data (**Fig. 1; Suppl. Fig. 1**) (28). As expected, the
256 largest subset of morphology DEGs (n = 730) was enriched in mature adipocytes, consistent with
257 central roles for adipocytes in defining overall adipose morphology (**Suppl. Fig. 1**). Notably, we also
258 identified 102 DEGs enriched in adipose stem and progenitor cells (ASPCs) (**Fig. 1; Suppl. Fig. 1; Suppl.**
259 **Table 2**). Given prior evidence that ASPC abundance and differentiation rate can influence adipose
260 tissue expansion and morphology (36,37), we hypothesised that these genes may function within
261 ASPCs to regulate or establish adipose morphology.

262

263 Analysis of candidate human adipose morphology genes using GWAS and cardiometabolic 264 trait associations

265 Prior to functional analysis, we first explored genetic and cardiometabolic features of the 102
266 candidate genes. As an initial step, we examined overlap with BMI- and WHR-associated GWAS
267 genes, and found that 16 of the candidate morphology genes were also BMI GWAS genes (*TNRC6B*,
268 *LRMDA*, *PRRX1*, *TSHZ2*, *PTPRD*, *PARD3*, *ADH1B*, *TBX15*, *MAGI2*, *RTL8A*, *CAST*, *BNC2*, *RERE*, *PTPRG*,
269 *ADAMTSL1* and *C1QBP*) and one gene, *HOXC4*, overlapped with WHR-associated loci; however,
270 Fisher's exact test indicated these overlaps were not significantly enriched (**Suppl. Fig. 2**). We next
271 clustered candidate genes based on their SAT expression correlations with 23 cardiometabolic traits
272 from the METSIM study (29). This revealed two distinct gene–trait signatures: one associated with a
273 "healthy" metabolic profile - characterised by higher hip circumference, fat-free mass, HDL-C, Muscle
274 Insulin Sensitivity Index (MISI) and adiponectin levels, alongside lower BMI, WHR, total fatty acids,
275 triacylglycerides, Insulin and HOMA-B - and another with an "unhealthy" profile, showing the
276 opposite trait pattern (**Suppl. Fig. 2**). Notably, genes associated with both hypertrophic and
277 hyperplastic adipose morphology were found across both signatures (**Suppl. Fig. 2**), suggesting that
278 these morphological phenotypes are not strictly aligned with traditional markers of metabolic health.

279

280 Enrichment of cell differentiation and developmental genes among adipose morphology 281 candidates

282 To explore functional themes within our gene set, we performed enrichment analysis to identify
283 overrepresented biological processes. This analysis revealed that 54 of the 102 ASPC-enriched genes
284 were significantly associated with Gene Ontology (GO) terms related to cell differentiation
285 (GO:0030154) and tissue development (GO:0048869, GO:0009888, GO:0032502) (**Figs. 1, 2A,B &**
286 **Suppl. Table 3**). Reasoning that they may play key roles in ASPC differentiation and/or the patterning
287 of adipose tissue, we prioritised this subset of 54 genes for further analysis. To refine this list, we
288 applied two complementary strategies. First, we ranked genes by their sequence conservation
289 between humans and zebrafish (**Fig. 2D**). Second, we assessed scRNA-Seq expression dynamics
290 during progenitor differentiation to adipocytes (38) (**Figs. 2D–F**). From this, we shortlisted 25 highly
291 conserved genes that were predominantly expressed in either progenitors from undifferentiated
292 samples, or within multipotent progenitors that persist following differentiation (*MGP+* SWAT cells)
293 (**Figs. 2D–F & Table 1).** This final set included genes with established roles in adipocyte progenitors –
294 such as *PRRX1* (H. Liu et al., 2022), *TBX15* (Pan et al., 2021), and *IRX1* (Han, 2022) - though their
295 specific contributions to adipose morphology have not yet been characterised.

296

297 An image-based pipeline to quantify lipid droplet size, number and spatial patterning in 298 zebrafish subcutaneous adipose

299 To investigate the function of the candidate morphology genes, we developed an image-based
300 phenotyping pipeline in zebrafish. Building on previous studies where Nile Red fluorescence was used
301 to quantify whole-animal adiposity and perform targeted CRISPR screens for regulators of total body
302 fat (16,26), we refined this approach to capture not only global adiposity data but also high-resolution
303 images of Nile Red-positive LDs. This enabled detailed quantification of LD size, number and spatial
304 patterning within zebrafish SAT (**Fig. 3A-D**). High-magnification images were acquired with a pixel
305 size between 1-2 μm^2 allowing individual LDs to be clearly resolved within zebrafish SAT (**Fig. 3A–D**).
306 Although very small LDs within multilocular adipocytes fall below our detection threshold, this
307 resolution reliably captures the larger LDs characteristic of mature adipocytes (**Fig. 3A-D**). Using this
308 pipeline, we characterised SAT development in 107 wild-type zebrafish from three independent
309 clutches (**Fig. 1E-G**). Representative LD masks illustrating the morphological progression of SAT
310 expansion are shown in **Fig. 3E**. Consistent with previous observations, LDs are first deposited at the
311 anterior end of the adipose depot and new LDs are added in both posterior and dorsoventral

312 directions (**Fig. 3E**). To spatially track this progression, we annotated the most anterior LD and defined
313 successive 200 µm strata extending posteriorly from this reference point (**Fig. 3E**). This stratification
314 enabled comparisons of LD morphology and number at anatomically and developmentally equivalent
315 positions across individuals. As zebrafish grew from 7 to 12 mm standard length (SL), we observed
316 limited increases in LD number within the anterior-most stratum (stratum 1) (**Fig. 3E & F**). Instead,
317 new LDs accumulated in more posterior regions, particularly in strata 3 and 4, which exhibited the
318 greatest LD number and overall growth (**Figs. 3E & F**). Concurrently, LDs increased in size, reaching
319 an average diameter of ~65 µm by 11–12 mm SL (**Fig. 3E & G**). Notably, posterior strata - containing
320 more recently formed LDs - appeared to be in the process of enlarging toward this consistent size
321 benchmark (**Fig. 3E & G**). Together, these findings show that during these relatively young juvenile
322 stages, LDs expand rapidly in size but ultimately stabilise at an average diameter of ~65 µm, reflecting
323 a potential upper limit of LD growth at this developmental stage.

324

325 Quantification of adipose morphology in juvenile zebrafish

326 As LD size, number and spatial dynamics can be robustly captured in juvenile zebrafish, we next
327 developed methodology to quantify adipose morphology – specifically hyperplastic versus
328 hypertrophic patterns – in a format scalable for CRISPR-based screening. Our approach was
329 conceptually based on previously described methods for assessing human adipose morphology (35).
330 To establish a baseline, we quantified SAT LD number and size within 194 wild-type fish (including
331 the 107 animals analysed in **Fig. 3**). We observed a strong curvilinear relationship between mean LD
332 diameter and the total depot size (R^2 = 0.85) (**Fig. 4A**). This relationship also held true for other LD
333 size metrics (including area and perimeter), further suggesting that as the zebrafish SAT expands, LDs
334 initially grow rapidly in size but then plateau as they reach a steady-state size and hypertrophic
335 growth slows relative to the overall size of the depot. Following the strategy of Arner et al (2010), we
336 calculated a 'morphology value' for each individual based on the deviation of each fish from the fitted
337 curve (**Fig. 4B**). Morphology values were normally distributed around zero, with approximately equal
338 proportions of individuals exhibiting hyperplastic (negative deviation) or hypertrophic (positive
339 deviation) SAT (**Fig. 4B**). Notably, morphology values were inversely correlated with LD number (p =
340 3.9×10^{-6}), such that hypertrophic individuals had fewer, larger LDs while hyperplastic individuals had

341 more numerous, smaller LDs (**Fig. 4C**). Together, these data show that morphology values can be
342 applied to zebrafish SAT and used to quantify hyperplastic/hypertrophic patterning.

343

344 Morphology values can be used to assess differences in F0 zebrafish CRISPR mutants

345 We next tested whether this metric could detect known regulators of adipose morphology. As a
346 positive control, we targeted *growth hormone 1* (*gh1)* using established F0 CRISPR mutant
347 methodology. Consistent with previous findings that *gh1* mutants display hypertrophic SAT LDs (39),
348 *gh1* F0 CRISPR mutants displayed significantly larger LDs and an upward shift in morphology values
349 ($p = 0.04$) (**Suppl. Fig. 3**). Notably, this effect was detected in only nine *gh1*-targeted fish,
350 corresponding to a large effect size (Cohen's $d = 1.06$) (**Suppl. Fig. 3**). Power analysis based on this
351 dataset indicated that similar effects could be detected with 80% power using as few as 11 fish.
352 Moreover, detecting medium-sized effects (Cohen's $d = 0.6$-0.7) would require only 23-31 mutant
353 fish. Together, these results demonstrate that image-based profiling of adipose morphology is a
354 sensitive and scalable approach for in vivo genetic screens aimed at identifying regulators of
355 hyperplastic and hypertrophic adipose growth.

356

357 A targeted CRISPR screen identified six genes that alter subcutaneous adipose morphology
358 in zebrafish

359 Following successful validation of our approach by targeting of *gh1*, we applied the same F0 CRISPR
360 methodology and image-based pipeline to functionally assess all 25 conserved candidate genes
361 identified from human adipose tissue datasets. Two independent experimental replicates were
362 performed for each gene target (**Table 1**), resulting in a total of 50 CRISPR targeting experiments and
363 1,393 juvenile zebrafish screened (**Table 1**). To quantify SAT morphology and classify hyperplastic or
364 hypertrophic profiles, we applied two complementary statistical approaches. First, we calculated
365 morphology values for each fish and compared mutant versus control morphology value distributions
366 using the Kolmogorov-Smirnov (KS) test. This non-parametric test does not assume a specific
367 distribution and is sensitive to shape-based distributional changes. Second, we applied linear mixed-
368 models (LMMs) to evaluate the relationship between LD size and total SAT area, whilst accounting
369 for replicate-specific variability. The LMMs allowed us to test whether LDs scaled normally with tissue

370 size (slope) or differed in size at any given adipose area (intercept). After correcting for multiple tests,
371 the KS test identified three mutants with hypertrophic morphology (*foxp1b*, *txnipa* and *mmp14b*) and
372 three with hyperplastic morphology (*ptenb*, *cxcl14* and *srpx*) (**Table 1 & Fig. 5**). Among the
373 hypertrophic mutants, *foxp1b* and *txnipa* were also detected using both LMMs for slope and
374 intercept, whilst *mmp14b* was only identified using the LMM for slope (**Table 1 & Fig. 5**). Conversely,
375 hyperplastic morphology in *ptenb*, *cxcl14* and *srpx* mutants was only detected using the KS test (**Table**
376 **1 & Fig. 5**). Interestingly, *ptenb* mutants exhibited both hyperplastic and hypertrophic populations of
377 LDs, suggesting a multimodal distribution of LDs (**Fig. 5A**). Together, these findings demonstrate
378 image-based profiling is an effective and scalable approach for identifying regulators of adipose
379 morphology.

380

gene target (zebrafish)	**sample size**		**Statistical power**			**KS test (FDR adjusted p value)**	**LMM – slope (FDR adjusted p value)**	**LMM – intercept (FDR adjusted p value)**
	expt.	**cont.**	**Small (0.4)**	**Medium (0.6)**	**Large (1)**			
prrx1b	51	57	54%	87%	99.9%	0.2652	0.979	0.871
foxp1b	36	57	46%	80%	99.6%	**0.02176**	**0.0022632**	**0.021712**
runx1t1	22	34	30%	58%	95%	0.4287	0.232961	0.306659
ptenb	25	29	30%	58%	95%	**0.006846**	0.674	0.508
cacnb4a	23	34	31%	59%	95%	0.6418	0.288296	0.463958
sparc	23	35	31%	59%	95.6%	0.293	0.557	0.767
pid1	26	29	31%	59%	95.3%	0.3481	0.10398	0.15810
sdk1a	25	34	32%	61%	96%	0.7517	0.534960	0.670365
cxcl14	24	29	30%	57%	94%	**0.02255**	0.462406	0.682372
ptprga	35	39	40%	72%	99%	0.4389	0.769939	0.810014
ptprdb	24	39	33%	62%	97%	0.203	0.212	0.450
lrmda	22	29	28%	55%	93%	0.966	0.181489	0.206508
txnipa	24	36	32%	61%	96%	**0.03319**	**3.10e-05**	**0.000923**
tmem115	29	29	32%	61%	96%	0.1469	0.224	0.187
tbx15	17	35	26%	51%	91%	0.3098	0.1416	0.1199
mmp14b	30	36	36%	67%	98%	**0.03856**	**0.00737**	0.07725
cd81a	26	35	33%	63%	97%	0.5928	0.160	0.198
aspa	17	17	20%	40%	81%	0.778		
srpx	20	25	26%	50%	90%	**0.02411**	0.263	0.201
pard3ab	32	42	39%	71%	99%	0.7033	0.545	0.592
nav3	28	42	37%	68%	98%	0.3718	0.199	0.258

lamb2	6	21	13%	24%	55%	0.7665		
kazna	23	42	33%	62%	97%	0.293	0.0774	0.0958

Table 1. Zebrafish gene targets and adipose morphology statistics. Adjusted p values after Benjamini-Hochberg FDR correction for 23 statistical tests. Small, medium and large correspond to effect sizes (Cohen's d). KS = Kolmogorov-Smirnov test. LMM = linear mixed model with experiment as random effect. Values in bold indicate statistical significance. All genes were targeted in two independent replicates (except for *aspa* and *lamb2* which only had a single replicate).

A hypertrophic growth bias of subcutaneous adipose in *foxp1b* and double *foxp1a;foxp1b* zebrafish mutants

Notably, targeting *foxp1b* (one of two zebrafish Foxp1 genes) induced hypertrophic SAT morphology (**Fig. 5**). Foxp1 is required for maintaining undifferentiated and self-renewing stem and progenitor cells in multiple tissue compartments (40–44). Further, in mouse, Foxp1 inhibits brown adipogenesis and browning of white adipocytes (45). However, roles for Foxp1 in establishing hyperplastic/hypertrophic morphology of adipose is unknown. To further study the role of Foxp1, we generated new loss-of-function alleles for both *foxp1* genes (*foxp1a* and *foxp1b*) in zebrafish (**Fig. 6A**). We targeted the highly conserved Forkhead domain (FHD) (**Fig. 6B**), which is essential for DNA binding and therefore Foxp1 transcriptional activity (46,47) (**Fig. 6B**). We generated two alleles – *foxp1a*^{ed116} and *foxp1b*^{ed125} – which each contained a frameshift and premature stop codon within the FHD (**Fig. 6B**). qRT-PCR revealed reduced *foxp1a* or *foxp1b* mRNA in the respective single mutants, with no apparent mRNA upregulation of the paralogous *foxp1* gene, or other members of the Foxp family (**Suppl. Fig. 4**). Western blots revealed a significant reduction of Foxp1 protein in each of the single mutants, and in *foxp1a;foxp1b* double mutants suggesting severe loss-of-function alleles (**Fig. 6C & Suppl. Fig. 4**). At approximately one-month of age (~10 mm SL), *foxp1b*^{ed125} and double *foxp1a;foxp1b* mutants were significantly smaller than either wild-type control or *foxp1a*^{ed116} fish (**Fig. 6E**), and analysis of baseline lipid storage within adipose tissues using Nile Red revealed that *foxp1b*^{ed125} and double *foxp1a;foxp1b* mutants also had lower lipid storage in adipose tissues than control fish (normalised to size of fish) (**Fig. 6F**). Similar to that observed in F0 CRISPR mutants, at one-month of age *foxp1b*^{ed125} and *foxp1a;foxp1b* mutants had significantly larger LDs characteristic of hypertrophic morphology (**Fig. 6G & H**). Analysis of blood metabolites revealed *foxp1a;foxp1b* double mutants were hyperglycaemic (**Suppl. Fig. 5**), and strikingly, in *foxp1a;foxp1b* double mutants there was increased lipid accumulation in the liver (**Fig. 6D & Suppl. Fig. 5D**). At adulthood, fish size and lipid storage within adipose in *foxp1a;foxp1b* double mutants had largely caught up with wild-

412 type control fish (adiposity at ~80% of wild-type levels) (**Suppl. Fig. 6**). These findings show that stable
413 *foxp1b* mutants have hypertrophic adipose along with metabolic dysfunction.

414

415 *foxp1b* zebrafish mutants are unable to undergo hypertrophic remodelling in response to a 416 high-fat diet

417 Our previous analyses showed that *foxp1b* mutants display a bias toward hypertrophic growth during
418 developmental expansion of SAT. To determine whether this bias impacts the adipose response to
419 dietary challenge, we subjected *foxp1a*, *foxp1b*, and *foxp1a;foxp1b* double mutants to a two-week
420 high-fat diet (HFD), a condition previously shown to induce SAT expansion (16). All *foxp1* mutant
421 genotypes exhibited reduced overall adipose expansion compared to control fish, indicating a general
422 impairment in expansion capacity (**Suppl. Fig. 7**). However, when LD diameter was assessed, a striking
423 difference emerged: the already hypertrophic SAT in *foxp1b* mutants failed to undergo further
424 hypertrophic remodelling in response to HFD (**Fig. 6J**). In contrast, *foxp1a* mutants, which did not
425 display a hypertrophic phenotype at baseline, demonstrated clear hypertrophic expansion following
426 HFD exposure (**Fig. 6J**). These findings suggest that the hypertrophic bias observed in *foxp1b* mutants
427 during development does not confer an enhanced capacity for hypertrophic remodelling during
428 dietary-induced adipose growth. Taken together, these results indicate that stable *foxp1b* and
429 *foxp1a;foxp1b* double mutants exhibit hypertrophic adipose morphology, but are unable to further
430 remodel hypertrophically in response to nutritional excess.

431

432 Discussion

433 In this study, we (i) identified candidate human genes implicated in hypertrophic and hyperplastic
434 remodelling of adipose tissue, (ii) established an image-based profiling method for assessing adipose
435 morphology in zebrafish, (iii) conducted an in vivo CRISPR screen in zebrafish to functionally evaluate
436 the roles of 25 candidate genes, (iv) identified six genes that influence hyperplastic or hypertrophic
437 remodelling, (v) focused on *Foxp1*, generating stable zebrafish mutant lines that recapitulate
438 phenotypes observed in F0 CRISPR experiments, and (vi) discovered that although *foxp1b* mutants
439 display baseline hypertrophic morphology, they fail to undergo further hypertrophic remodelling in
440 response to a high-fat diet, suggesting that a developmental bias in adipose growth influences later

441 responses to diet. Together, this work demonstrates a scalable, tractable screening platform to
442 identify regulators of adipose remodelling.

443

444 In this study we employed a multi-step process to identify candidate morphology genes from human
445 data. As GWAS for adipose morphology has only been conducted in relatively small cohorts (48,49),
446 we instead used published transcriptomic data that identified DEGs enriched in SAT characterised by
447 large or small adipocytes (27). Clustering of the morphology DEG expression correlations with
448 cardiometabolic traits separated genes into 'healthy' and 'unhealthy' profiles (**Suppl. Fig. 2**); genes
449 associated with larger adipocytes generally aligned with adverse metabolic traits such as increased
450 BMI and WHR in accordance with adipocyte size increasing with BMI (50). However, this pattern was
451 not absolute—some candidates diverged from this axis (**Suppl. Fig. 2**), representing potentially
452 interesting regulators of adipose morphology that are uncoupled from traditional metabolic or
453 disease states. For this study, we focussed on candidate genes that were highly expressed or enriched
454 within adipocyte stem and progenitor cells (ASPCs), wanting to focus on the hyperplastic potential of
455 adipose influencing remodelling capacity and mechanism. However, we note that hyperplastic
456 adipose potential is likely determined by multiple cell types, not just progenitors, and also including
457 the adipose microenvironment (51,52).

458

459 We established a rapid, scalable, stereomicroscope-based imaging pipeline for profiling zebrafish
460 adipose morphology. Our imaging resolution was sufficient to detect large LDs but not smaller LDs
461 found as secondary LDs in zebrafish adipocytes (52), a phenomenon which is also found in mouse
462 adipocytes (53). Nevertheless, our methodology reliably captured large LDs and allowed us to use LD
463 size as a proxy for overall adipocyte size. We adapted an existing analytical framework from the Arner
464 lab, applying morphology value metrics developed for human adipose tissue to zebrafish SAT, and
465 observed very similar relationships, including a curvilinear relationship between LD size and depot
466 size and an inverse correlation between LD number and LD size. We therefore believe that the growth
467 dynamics of zebrafish adipose is likely similar to that of mammals. To test for differences in adipose
468 morphology, we implemented two complementary statistical approaches: the Kolmogorov–Smirnov
469 (KS) test to compare the overall distribution of morphology values between groups, and linear mixed
470 models (LMMs) to assess group-specific changes in LD size while accounting for experimental batch

471 effects. The KS test proved more sensitive to subtle distributional shifts, while the LMMs provided a
472 more conservative measure of structured group-level differences. This dual-method strategy is well-
473 suited for future high-throughput screens, including those targeting GWAS-derived candidates.

474

475 Using this platform, we identified six mutants that altered adipose morphology. *Txnipa (txnipa)* F0
476 CRISPR mutants displayed hypertrophic morphology. TXNIP (Thioredoxin-Interacting Protein) is a
477 well-characterised regulator of oxidative stress, metabolism, and inflammation. TXNIP binds and
478 inhibits the antioxidant thioredoxin, leading to increased production of reactive oxygen species and
479 oxidative stress (54). Interestingly TXNIP links nutrient sensing to inflammatory signalling by
480 responding to and regulating glucose uptake and NLRP3 inflammasome complex formation (54).
481 Interestingly, the ROS/TXNIP/NLRP3 pathway impairs insulin signalling, a major driver of
482 adipogenesis and hyperplastic adipose growth (55). Further, vitamin D increases TXNIP expression
483 (56), which plays a major role in energy storage in zebrafish (57). *Mmp14b* F0 zebrafish mutants also
484 exhibited hypertrophic adipose. MMP14 (Matrix Metallopeptidase 14) is a pericellular collagenase
485 and plays a key role in ECM remodelling. In mice, MMP14 deficiency stiffens the adipose matrix and
486 restricts hypertrophic expansion, resulting in adipose characterised by small adipocytes (58).
487 Conversely, overexpression of Mmp14 increased the size of adipocytes (59). As such, these mouse
488 phenotypes appear contradictory to the hypertrophic morphology we observe after mutation of
489 *mmp14b* in zebrafish and warrant further investigation. We note that two *mmp14* genes exist in
490 zebrafish, therefore both paralogues could be targeted in future studies. *Ptenb* F0 zebrafish mutants
491 predominantly showed a hyperplastic phenotype, however a population of hypertrophic LDs were
492 also present suggesting a bimodal size distribution. PTEN (Phosphatase and Tensin homolog) inhibits
493 PI3K/AKT signalling and loss in progenitor cells promotes differentiation and hyperplastic growth in
494 line with formation of lipomas in patients with PTEN hamartoma tumour syndrome (60).
495 Interestingly, PTEN knockout mouse models also appear to show bimodal adipocyte sizes in gonadal
496 and retroperitoneal adipose, suggesting that complex adipose expansion dynamics are controlled by
497 PTEN (61). *Cxcl14* F0 zebrafish mutants also displayed a hyperplastic phenotype. CXCL14 is a
498 chemokine and adipokine that regulates immune tone and progenitor dynamics in adipose tissue.
499 Circulating *CXCL14* mRNA was decreased in obesity, and inversely correlated with pro-inflammatory
500 pathway members, and positively correlated with GLUT4 and Adiponectin suggesting a dysregulated
501 metabolic and inflammatory state (62).

502

503 Of great interest, *srpx* F0 CRISPR mutants showed a hyperplastic SAT morphology. Interetsngly, SRPX
504 has not been previously shown to have a role in adipose tissue, however it is part of the
505 transcriptomic signature of CD142+ ASPCs in mouse, which function as non-adipogenic inhibitors of
506 adipogenesis (Aregs) (63). It is therefore of interest to test whether Srpx functions within Aregs to
507 regulate hyperplastic remodelling, with a reduction of Srpx leading to increased hyperplastic growth.
508 Outside of adipose, Srpx is implicated in the negative regulation of cell proliferation and has is a
509 marker gene for glioblastoma (64).

510

511 For the primary functional follow-up in this study, we focused on *Foxp1*, a gene known to maintain
512 stem and progenitor populations in multiple tissues including the hair follicle, haematopoietic niche,
513 mammary gland, and cerebral cortex (40,41,43,44). We hypothesise that *Foxp1* may be required in
514 adipose progenitors for hyperplastic growth, and that its loss would result in compensatory
515 hypertrophy. In mouse models, *Foxp1* deletion leads to increased browning of white adipose tissue
516 and enhanced thermogenesis (45), suggesting a repressive role in thermogenic programming.
517 Although zebrafish are ectothermic and historically not thought to possess thermogenic adipocytes,
518 recent evidence shows epicardial adipose in zebrafish is thermogenic (15), raising the possibility that
519 *foxp1* mutants may also undergo browning—an intriguing hypothesis for future work. We generated
520 stable *foxp1a* and *foxp1b* mutant lines carrying severe loss-of-function alleles, confirmed by reduced
521 protein expression. *Foxp1b* mutants displayed more severe phenotypes than *foxp1a*, consistent with
522 its higher conservation with mammalian *FOXP1*. The major phenotype in *foxp1a* mutants was
523 impaired adipose expansion following HFD, suggesting failure to respond to diet-induced stress
524 signals. In contrast, *foxp1b* mutants were smaller at baseline, with less adipose tissue, along with a
525 failure to expand adipose following a HFD. Notably, the double mutants developed fatty liver and
526 hyperglycaemia—phenotypes also observed in *Foxp1*-deficient mice (65), where increased hepatic
527 de novo lipogenesis (DNL) contributes to ectopic fat deposition and disrupted glucose homeostasis.
528 This may similarly underlie the zebrafish phenotype and could be tested in future work.

529

530 Strikingly, despite *foxp1b* mutants displaying a baseline bias towards hypertrophy, they were unable
531 to undergo further hypertrophic expansion in response to HFD. This contrasts with *foxp1a* mutants,

532 which readily increased LD size post-diet. The inability of *foxp1b* mutants to undergo diet-induced
533 hypertrophic remodelling suggests a potential ceiling effect on adipocyte size, possibly due to
534 physical or molecular constraints. As all experiments were conducted in growing juveniles, this may
535 reflect developmental limitations—such as restricted compartment space or altered ECM properties.
536 Alternatively, *foxp1b* mutants may fail to perceive or respond to HFD-induced molecular cues,
537 potentially implicating *Foxp1* in metabolic sensing(66). It remains to be determined whether this is a
538 *foxp1b*-specific effect or if a general developmental bias towards hypertrophy limits later
539 hypertrophic remodelling which could be tested in the other hypertrophic mutants identified in this
540 screen.

541

542 Acknowledgements

543 We thank Rosalyn Fong for help with initial zebrafish *foxp1* genotyping strategies, and David Duneau,
544 Will Cawthorn and Rob Semple for advice on modelling of adipose morphology. The work was funded
545 by a British Heart Foundation PhD Studentship awarded to RW, and a BBSRC grant (BB/X009467/1)
546 awarded to PT and JENM.

547

548 Author contributions

549 RW and PT performed experiments, RW, PT and JENM performed data analysis, PT and JENM wrote
550 the manuscript.

551 **REFERENCES**

552 1. Tandon P, Wafer R, Minchin JEN. Adipose morphology and metabolic disease. J Exp Biol. 2018 Mar
553 7;221(Pt Suppl 1):jeb164970.

554 2. Hagberg CE, Spalding KL. White adipocyte dysfunction and obesity-associated pathologies in humans. Nat
555 Rev Mol Cell Biol. 2024 Apr;25(4):270–89.

556 3. Vishvanath L, Gupta RK. Contribution of adipogenesis to healthy adipose tissue expansion in obesity. J
557 Clin Invest. 2019 Oct 1;129(10):4022–31.

558 4. Rydén M, Arner P. Cardiovascular risk score is linked to subcutaneous adipocyte size and lipid metabolism.
559 J Intern Med. 2017 Sep;282(3):220–8.

560 5. Acosta JR, Douagi I, Andersson DP, Bäckdahl J, Rydén M, Arner P, et al. Increased fat cell size: a major
561 phenotype of subcutaneous white adipose tissue in non-obese individuals with type 2 diabetes.
562 Diabetologia. 2016 Mar;59(3):560–70.

563 6. Weyer C, Foley JE, Bogardus C, Tataranni PA, Pratley RE. Enlarged subcutaneous abdominal adipocyte
564 size, but not obesity itself, predicts type II diabetes independent of insulin resistance. Diabetologia. 2000
565 Dec;43(12):1498–506.

566 7. Hoffstedt J, Arner E, Wahrenberg H, Andersson DP, Qvisth V, Löfgren P, et al. Regional impact of adipose
567 tissue morphology on the metabolic profile in morbid obesity. Diabetologia. 2010 Dec;53(12):2496–503.

568 8. Boden G, Cheung P, Mozzoli M, Fried SK. Effect of thiazolidinediones on glucose and fatty acid metabolism
569 in patients with type 2 diabetes. Metabolism. 2003 Jun;52(6):753–9.

570 9. Kim SM, Lun M, Wang M, Senyo SE, Guillermier C, Patwari P, et al. Loss of white adipose hyperplastic
571 potential is associated with enhanced susceptibility to insulin resistance. Cell Metab. 2014 Dec
572 2;20(6):1049–58.

573 10. Gao Z, Daquinag AC, Fussell C, Zhao Z, Dai Y, Rivera A, et al. Age-associated telomere attrition in adipocyte
574 progenitors predisposes to metabolic disease. Nat Metab. 2020 Dec;2(12):1482–97.

575 11. Muir LA, Neeley CK, Meyer KA, Baker NA, Brosius AM, Washabaugh AR, et al. Adipose tissue fibrosis,
576 hypertrophy, and hyperplasia: Correlations with diabetes in human obesity. Obesity . 2016
577 Mar;24(3):597–605.

578 12. Arner P, Arner E, Hammarstedt A, Smith U. Genetic predisposition for Type 2 diabetes, but not for
579 overweight/obesity, is associated with a restricted adipogenesis. PLoS One. 2011 Apr 12;6(4):e18284.

580 13. Flynn EJ 3rd, Trent CM, Rawls JF. Ontogeny and nutritional control of adipogenesis in zebrafish (Danio
581 rerio). J Lipid Res. 2009 Aug;50(8):1641–52.

582 14. Imrie D, Sadler KC. White adipose tissue development in zebrafish is regulated by both developmental
583 time and fish size. Dev Dyn. 2010 Nov;239(11):3013–23.

584 15. Morocho-Jaramillo P-A, Kotlar-Goldaper I, Zakarauskas-Seth BI, Purfürst B, Filosa A, Sawamiphak S. The
585 zebrafish heart harbors a thermogenic beige fat depot analog of human epicardial adipose tissue. Cell
586 Rep. 2024 Mar 26;43(3):113955.

587 16. Minchin JEN, Rawls JF. A classification system for zebrafish adipose tissues. Dis Model Mech. 2017 Jun
588 1;10(6):797–809.

589 17. Minchin JEN, Scahill CM, Staudt N, Busch-Nentwich EM, Rawls JF. Deep phenotyping in zebrafish reveals
590 genetic and diet-induced adiposity changes that may inform disease risk. J Lipid Res. 2018
591 Aug;59(8):1536–45.

592 18. Oka T, Nishimura Y, Zang L, Hirano M, Shimada Y, Wang Z, et al. Diet-induced obesity in zebrafish shares
593 common pathophysiological pathways with mammalian obesity. BMC Physiol. 2010 Oct 21;10(1):21.

594 19. Landgraf K, Schuster S, Meusel A, Garten A, Riemer T, Schleinitz D, et al. Short-term overfeeding of
595 zebrafish with normal or high-fat diet as a model for the development of metabolically healthy versus
596 unhealthy obesity. BMC Physiol. 2017 Mar 21;17(1):4.

597 20. Minchin JEN, Rawls JF. In vivo analysis of white adipose tissue in zebrafish. Methods Cell Biol.
598 2011;105:63–86.

599 21. Lumaquin D, Johns E, Montal E, Weiss JM, Ola D, Abuhashem A, et al. An in vivo reporter for tracking lipid
600 droplet dynamics in transparent zebrafish. Elife [Internet]. 2021 Jun 11;10. Available from:
601 https://pubmed.ncbi.nlm.nih.gov/34114952/

602 22. Wilson MH, Ekker SC, Farber SA. Imaging cytoplasmic lipid droplets in vivo with fluorescent perilipin 2
603 and perilipin 3 knock-in zebrafish. Elife [Internet]. 2021 Aug 13;10. Available from:
604 https://pubmed.ncbi.nlm.nih.gov/34387191/

605 23. Lepanto P, Levin-Ferreyra F, Koziol U, Malacrida L, Badano JL. Insights into in vivo adipocyte
606 differentiation through cell-specific labeling in zebrafish. Biol Open [Internet]. 2021 Sep 15;10(9).
607 Available from: http://dx.doi.org/10.1242/bio.058734

608 24. Mao Y, Hong K-H, Liao W, Li L, Kim S-J, Xiong Y, et al. Generation of a novel transgenic zebrafish for
609 studying adipocyte development and metabolic control. Int J Mol Sci. 2021 Apr 13;22(8):3994.

610 25. Mazzaferro E, Mujica E, Zhang H, Emmanouilidou A, Jenseit A, Evcimen B, et al. Functionally characterizing
611 obesity-susceptibility genes using CRISPR/Cas9, in vivo imaging and deep learning. Sci Rep. 2025 Feb
612 13;15(1):5408.

613 26. van der Klaauw AA, Croizier S, Mendes de Oliveira E, Stadler LKJ, Park S, Kong Y, et al. Human Semaphorin
614 3 variants link melanocortin circuit development and energy balance. Cell. 2019 Feb 7;176(4):729-
615 742.e18.

616 27. Honecker J, Ruschke S, Seeliger C, Laber S, Strobel S, Pröll P, et al. Transcriptome and fatty-acid signatures
617 of adipocyte hypertrophy and its non-invasive MR-based characterization in human adipose tissue.
618 EBioMedicine. 2022 May;79:104020.

619 28. Emont MP, Jacobs C, Essene AL, Pant D, Tenen D, Colleluori G, et al. A single-cell atlas of human and
620 mouse white adipose tissue. Nature. 2022 Mar;603(7903):926–33.

621 29. Civelek M, Wu Y, Pan C, Raulerson CK, Ko A, He A, et al. Genetic Regulation of Adipose Gene Expression
622 and Cardio-Metabolic Traits. Am J Hum Genet. 2017 Mar 2;100(3):428–43.

623 30. Kroll F, Powell GT, Ghosh M, Gestri G, Antinucci P, Hearn TJ, et al. A simple and effective F0 knockout
624 method for rapid screening of behaviour and other complex phenotypes. Elife [Internet]. 2021 Jan 8;10.
625 Available from: http://dx.doi.org/10.7554/eLife.59683

626 31. Varshney GK, Pei W, LaFave MC, Idol J, Xu L, Gallardo V, et al. High-throughput gene targeting and
627 phenotyping in zebrafish using CRISPR/Cas9. Genome Res. 2015 Jul;25(7):1030–42.

628 32. Wu RS, Lam II, Clay H, Duong DN, Deo RC, Coughlin SR. A Rapid Method for Directed Gene Knockout for
629 Screening in G0 Zebrafish. Dev Cell. 2018 Jul 2;46(1):112-125.e4.

630 33. Stringer C, Wang T, Michaelos M, Pachitariu M. Cellpose: a generalist algorithm for cellular segmentation.
631 Nat Methods. 2021 Jan;18(1):100–6.

632 34. Tandon P, Lyall Z, Cowie M, Minchin JEN. Human genetic studies and zebrafish models identify Plxna4 as
633 a regulator of adiposity, somatic growth, and feeding behaviours [Internet]. bioRxiv. 2025 [cited 2025 Apr
634 18]. p. 2025.03.15.643290. Available from:
635 https://www.biorxiv.org/content/10.1101/2025.03.15.643290v1.abstract

636 35. Arner E, Westermark PO, Spalding KL, Britton T, Rydén M, Frisén J, et al. Adipocyte turnover: relevance
637 to human adipose tissue morphology. Diabetes. 2010 Jan;59(1):105–9.

638 36. Gustafson B, Nerstedt A, Smith U. Reduced subcutaneous adipogenesis in human hypertrophic obesity is
639 linked to senescent precursor cells. Nat Commun. 2019 Jun 21;10(1):2757.

640 37. Hedbacker K, Lu Y-H, Dallner O, Li Z, Fayzikhodjaeva G, Birsoy K, et al. Limitation of adipose tissue by the
641 number of embryonic progenitor cells. Elife [Internet]. 2020 May 26;9. Available from:
642 http://dx.doi.org/10.7554/eLife.53074

643 38. Yang Loureiro Z, Joyce S, DeSouza T, Solivan-Rivera J, Desai A, Skritakis P, et al. Wnt signaling preserves
644 progenitor cell multipotency during adipose tissue development. Nat Metab. 2023 Jun;5(6):1014–28.

645 39. McMenamin SK, Minchin JEN, Gordon TN, Rawls JF, Parichy DM. Dwarfism and increased adiposity in the
646 gh1 mutant zebrafish vizzini. Endocrinology. 2013 Apr 1;154(4):1476–87.

647 40. Zhao J, Li H, Zhou R, Ma G, Dekker JD, Tucker HO, et al. Foxp1 regulates the proliferation of hair follicle
648 stem cells in response to oxidative stress during hair cycling. PLoS One. 2015 Jul 14;10(7):e0131674.

649 41. Naudin C, Hattabi A, Michelet F, Miri-Nezhad A, Benyoucef A, Pflumio F, et al. PUMILIO/FOXP1 signaling
650 drives expansion of hematopoietic stem/progenitor and leukemia cells. Blood. 2017 May
651 4;129(18):2493–506.

652 42. Li H, Liu P, Xu S, Li Y, Dekker JD, Li B, et al. FOXP1 controls mesenchymal stem cell commitment and
653 senescence during skeletal aging. J Clin Invest. 2017 Apr 3;127(4):1241–53.

654 43. Pearson CA, Moore DM, Tucker HO, Dekker JD, Hu H, Miquelajáuregui A, et al. Foxp1 regulates neural
655 stem cell self-renewal and bias toward deep layer cortical fates. Cell Rep. 2020 Feb 11;30(6):1964-
656 1981.e3.

657 44. Fu NY, Pal B, Chen Y, Jackling FC, Milevskiy M, Vaillant F, et al. Foxp1 Is Indispensable for Ductal
658 Morphogenesis and Controls the Exit of Mammary Stem Cells from Quiescence. Dev Cell. 2018 Dec
659 3;47(5):629-644.e8.

660 45. Liu P, Huang S, Ling S, Xu S, Wang F, Zhang W, et al. Foxp1 controls brown/beige adipocyte differentiation
661 and thermogenesis through regulating β3-AR desensitization. Nat Commun. 2019 Nov 7;10(1):5070.

662 46. Dai S, Qu L, Li J, Chen Y. Toward a mechanistic understanding of DNA binding by forkhead transcription
663 factors and its perturbation by pathogenic mutations. Nucleic Acids Res. 2021 Oct 11;49(18):10235–49.

664 47. Stroud JC, Wu Y, Bates DL, Han A, Nowick K, Paabo S, et al. Structure of the forkhead domain of FOXP2
665 bound to DNA. Structure. 2006 Jan;14(1):159–66.

666 48. Glastonbury CA, Pulit SL, Honecker J, Censin JC, Laber S, Yaghootkar H, et al. Machine Learning based
667 histology phenotyping to investigate the epidemiologic and genetic basis of adipocyte morphology and
668 cardiometabolic traits. PLoS Comput Biol. 2020 Aug;16(8):e1008044.

669 49. Kulyté A, Aman A, Strawbridge RJ, Arner P, Dahlman IA. Genome-wide association study identifies genetic
670 loci associated with fat cell number and overlap with genetic risk loci for type 2 diabetes. Diabetes. 2022
671 Jun 1;71(6):1350–62.

672 50. Ye RZ, Richard G, Gévry N, Tchernof A, Carpentier AC. Fat cell size: Measurement methods,
673 pathophysiological origins, and relationships with metabolic dysregulations. Endocr Rev. 2022 Jan
674 12;43(1):35–60.

675 51. Jeffery E, Wing A, Holtrup B, Sebo Z, Kaplan JL, Saavedra-Peña R, et al. The adipose tissue
676 microenvironment regulates depot-specific adipogenesis in obesity. Cell Metab. 2016 Jul 12;24(1):142–
677 50.

678 52. Minchin JEN, Dahlman I, Harvey CJ, Mejhert N, Singh MK, Epstein JA, et al. Plexin D1 determines body fat
679 distribution by regulating the type V collagen microenvironment in visceral adipose tissue. Proc Natl Acad
680 Sci U S A. 2015 Apr 7;112(14):4363–8.

681 53. Chau Y-Y, Bandiera R, Serrels A, Martínez-Estrada OM, Qing W, Lee M, et al. Visceral and subcutaneous
682 fat have different origins and evidence supports a mesothelial source. Nat Cell Biol. 2014 Apr;16(4):367–
683 75.

684 54. Choi E-H, Park S-J. TXNIP: A key protein in the cellular stress response pathway and a potential therapeutic
685 target. Exp Mol Med. 2023 Jul 3;55(7):1348–56.

686 55. Russell-Guzmán J, Américo-Da Silva L, Cadagan C, Maturana M, Palomero J, Estrada M, et al. Activation
687 of the ROS/TXNIP/NLRP3 pathway disrupts insulin-dependent glucose uptake in skeletal muscle of
688 insulin-resistant obese mice. Free Radic Biol Med. 2024 Sep 1;222:187–98.

689 56. Hamilton JP, Potter JJ, Koganti L, Meltzer SJ, Mezey E. Effects of vitamin D3 stimulation of thioredoxin-
690 interacting protein in hepatocellular carcinoma: TXNIP, vitamin D3 and HCC. Hepatol Res. 2014
691 Dec;44(13):1357–66.

692 57. Freeburg SH, Shwartz A, Kemény LV, Smith CJ, Weeks O, Miller BM, et al. Hepatocyte vitamin D receptor
693 functions as a nutrient sensor that regulates energy storage and tissue growth in zebrafish. Cell Rep. 2024
694 Jul 23;43(7):114393.

695 58. Chun T-H, Hotary KB, Sabeh F, Saltiel AR, Allen ED, Weiss SJ. A pericellular collagenase directs the 3-
696 dimensional development of white adipose tissue. Cell. 2006 May 5;125(3):577–91.

697 59. Li X, Zhao Y, Chen C, Yang L, Lee H-H, Wang Z, et al. Critical role of matrix metalloproteinase 14 in adipose
698 tissue remodeling during obesity. Mol Cell Biol. 2020 Mar 30;40(8):1–24.

699 60. Kirstein AS, Kehr S, Nebe M, Hanschkow M, Barth LAG, Lorenz J, et al. PTEN regulates adipose progenitor
700 cell growth, differentiation, and replicative aging. J Biol Chem. 2021 Aug;297(2):100968.

701 61. Huang W, Queen NJ, McMurphy TB, Ali S, Cao L. Adipose PTEN regulates adult adipose tissue homeostasis
702 and redistribution via a PTEN-leptin-sympathetic loop. Mol Metab. 2019 Dec;30:48–60.

703 62. Cereijo R, Quesada-López T, Gavaldà-Navarro A, Tarascó J, Pellitero S, Reyes M, et al. The chemokine
704 CXCL14 is negatively associated with obesity and concomitant type-2 diabetes in humans. Int J Obes .
705 2021 Mar;45(3):706–10.

706 63. Zachara M, Rainer PY, Hashimi H, Russeil JM, Alpern D, Ferrero R, et al. Mammalian adipogenesis
707 regulator (Areg) cells use retinoic acid signalling to be non- and anti-adipogenic in age-dependent
708 manner. EMBO J. 2022 Sep 15;41(18):e108206.

709 64. Ampudia-Mesias E, El-Hadad S, Cameron CS, Wöhrer A, Ströbel T, Saydam N, et al. SRPX emerges as a
710 potential tumor marker in the extracellular vesicles of glioblastoma. Cancers (Basel). 2022 Apr
711 14;14(8):1984.

712 65. Zou Y, Gong N, Cui Y, Wang X, Cui A, Chen Q, et al. Forkhead box P1 (FOXP1) transcription factor regulates
713 hepatic glucose homeostasis. J Biol Chem. 2015 Dec 18;290(51):30607–15.

714 66. Ma H, Sukonina V, Zhang W, Meng F, Subhash S, Palmgren H, et al. The transcription factor Foxp1
715 regulates aerobic glycolysis in adipocytes and myocytes. J Biol Chem. 2023 May 5;104795.

716

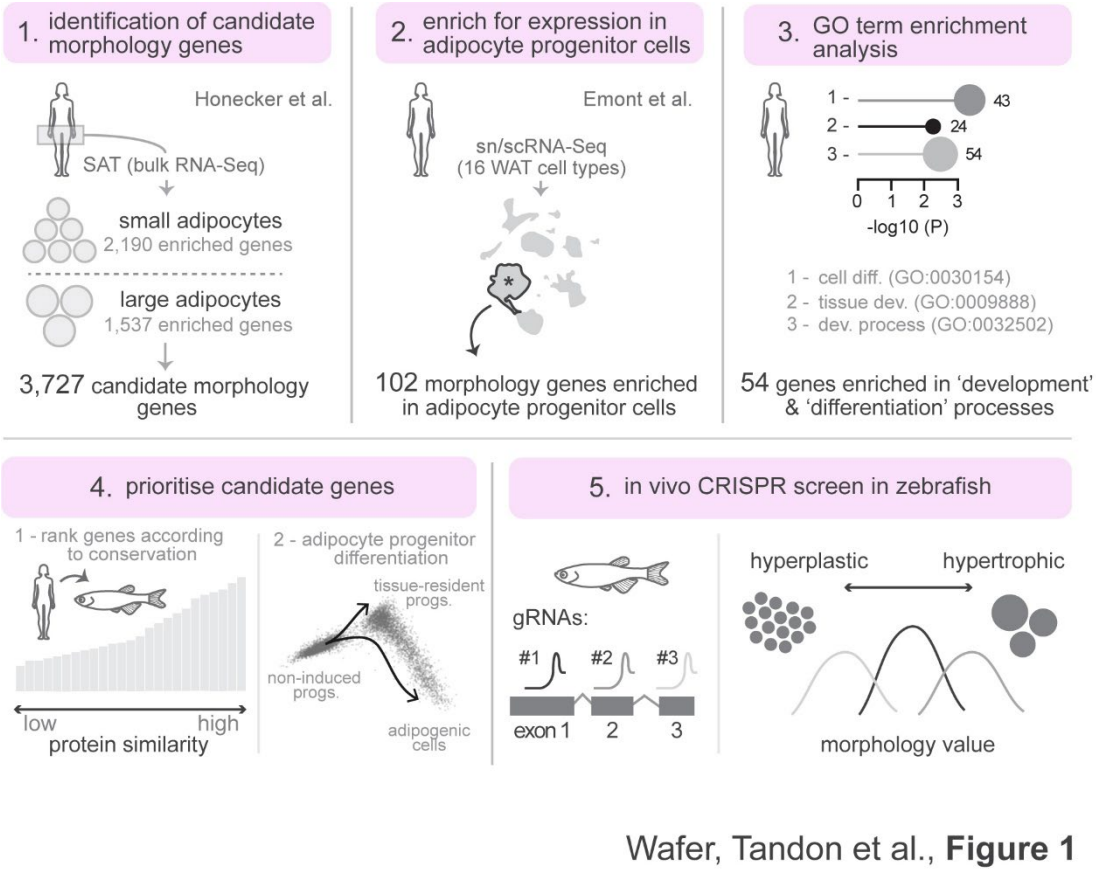

Wafer, Tandon et al., **Figure 1**

Figure 1. Project overview. Depicting steps for candidate gene identification based on human transcriptomic data (1), enriching for genes expressed within adipose stem and progenitor cells, (3) GO term enrichment analysis of candidate genes to focus on development and differentiation processes, (4) prioritisation of candidate genes based on conservation to zebrafish and expression dynamics during adipocyte progenitor differentiation and (5) an in vivo CRISPR screen in zebrafish to functionally characterise genes.

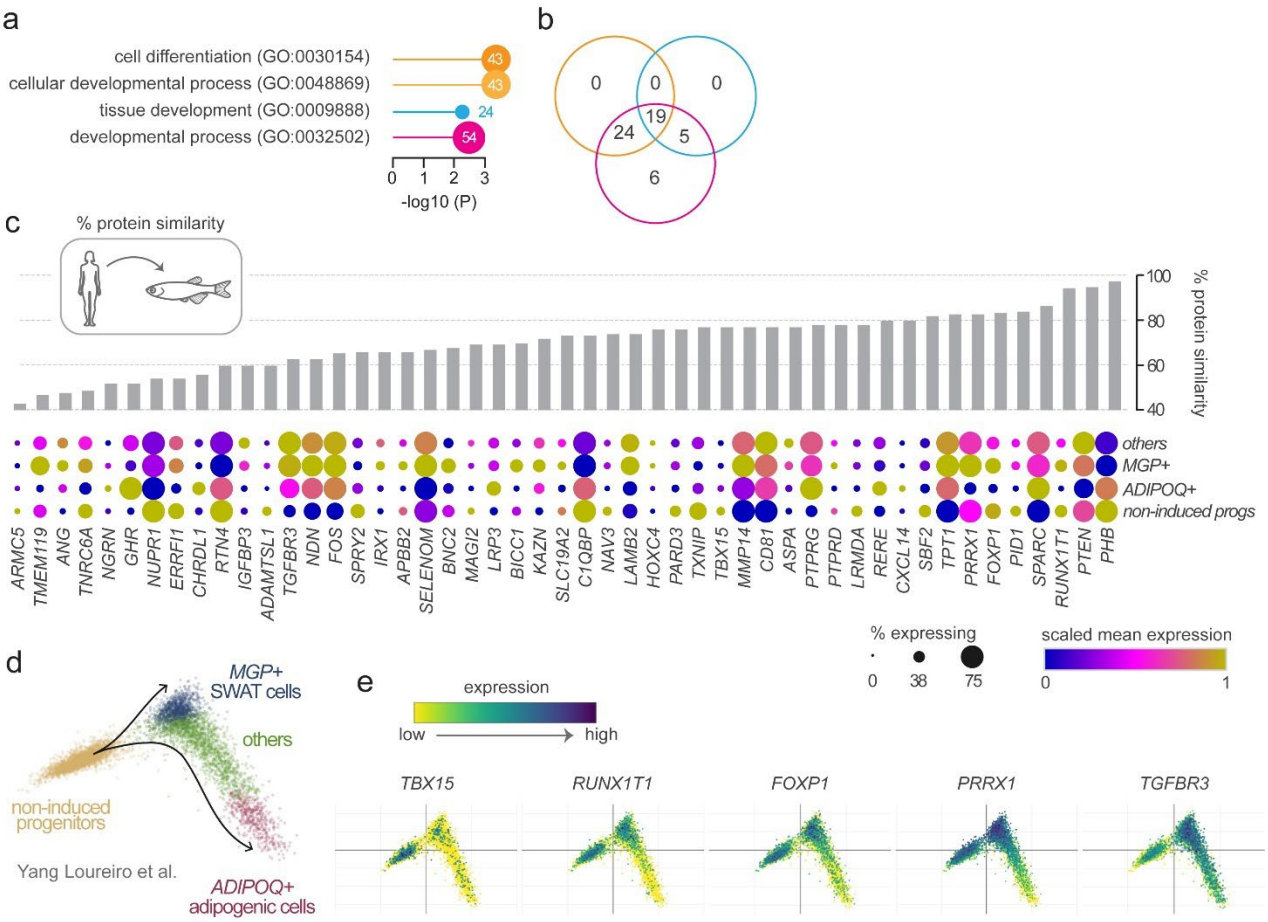

Wafer, Tandon et al., **Figure 2**

Figure 2. Prioritisation of candidate adipose morphology genes based on conservation to zebrafish and expression dynamics during progenitor differentiation. A. GO term enrichment analysis of the 102 candidate morphology genes enriched in adipose stem and progenitor cells. 54 of these genes were enriched in four GO terms related to development and differentiation. **B.** Venn diagram showing gene intersection between GO terms. Cell differentiation (GO:0030154) and cellular developmental process (GO:0048869) had 100% overlap. **C.** Grey bars denote % protein similarity between human and zebrafish orthologs. Dot plots below show scaled mean expression (colour) and % of cells expressing (dot size) each candidate genes within four cell types identified during progenitor differentiation to adipocytes. Cell types are: non-induced progenitors, *MGP+* SWAT cells, *ADIPOQ+* adipogenic cells and others, based on Yang Loureiro et al., 2023. **D.** PCA projection of single cells according to cluster designation from C. **E.** Example candidate morphology genes and their expression during adipocyte differentiation.

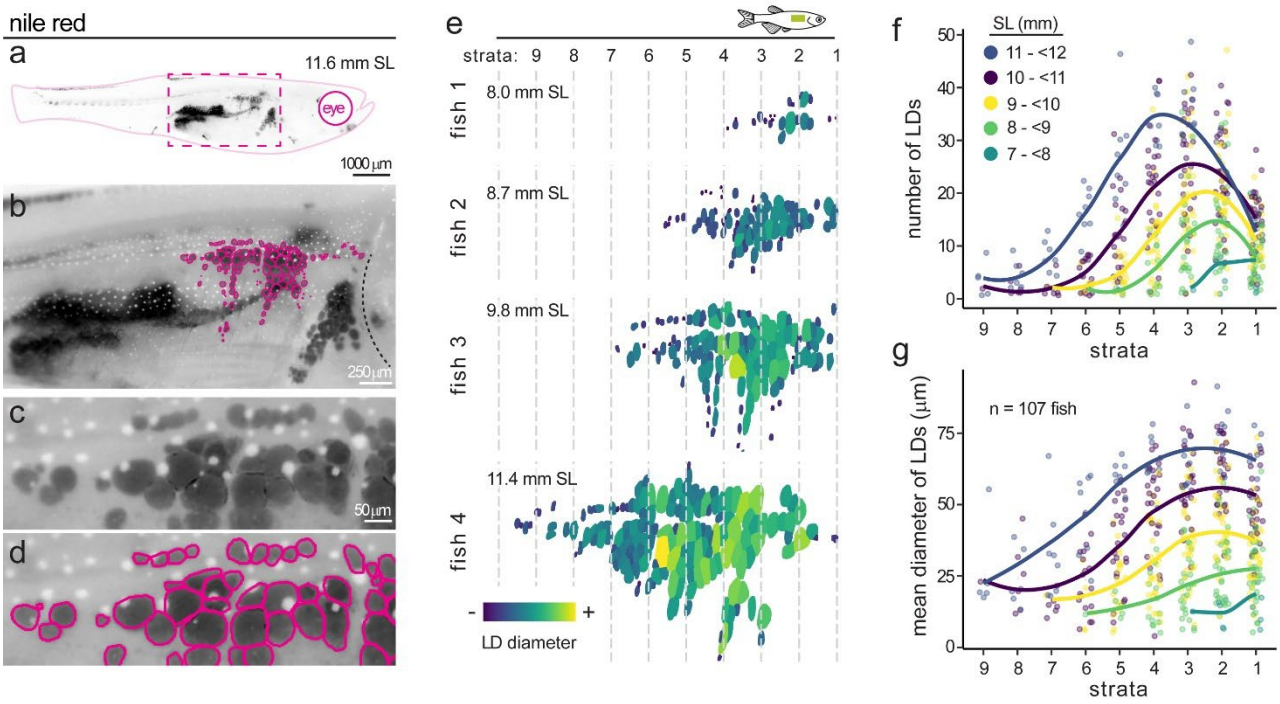

Figure 3. Spatial dynamics of subcutaneous adipose growth in zebrafish. A. Nile Red stained zebrafish at 11.6 mm standard length (SL). Black signal denotes Nile Red+ neutral lipid within adipose. The magenta dotted box denotes the area shown in B. **B.** Higher magnification image showing region of interest. Magenta outlined lipid droplets (LDs) highlight the subcutaneous adipose tissue. **C.** Zoomed in view of subcutaneous adipose LDs. White dots are melanosome pigment granules. **D.** Magenta liens outline the LD segmentation performed on LDs from C. **E.** Segmented subcutaneous adipose LDs colour-coded according to LD diameter from four representative zebrafish at different sizes. Fish sizes are shown in mm SL. Strata were defined in 200 µm intervals from the most anterior (to the right) LD. **F.** Number of LDs in each strata according to size of the zebrafish (SL). Zebrafish were categorised into 5 groups according to size. **G.** Mean diameter of LDs in each strata according to size of zebrafish.

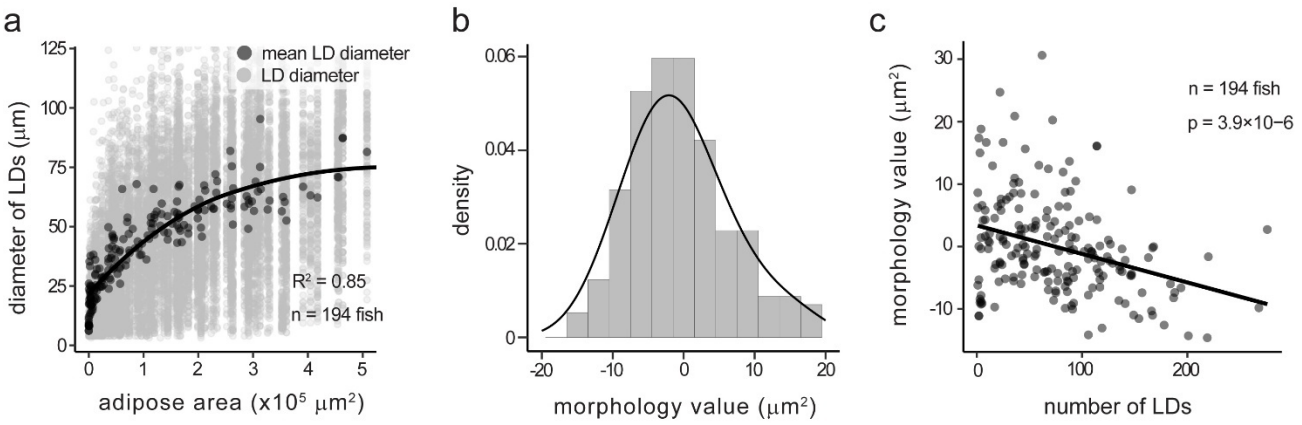

Wafer, Tandon et al., **Figure 4**

Figure 4. Calculation of adipose morphology value based on relationship between lipid droplet size and overall adipose depot size. A. Diameter of subcutaneous adipose LDs plotted relative to depot area. Mean LD diameters per fish are dark grey, individual LD diameters are light grey. Line was fitted using a generalised additive model. **B.** Morphology values were calculated as the deviation of mean LD diameter from the fitted model in A. Note the normal distribution of morphology values around zero. **C.** Inverse relationship between morphology value and number of LDs. A linear model was fitted to show the inverse relationship.

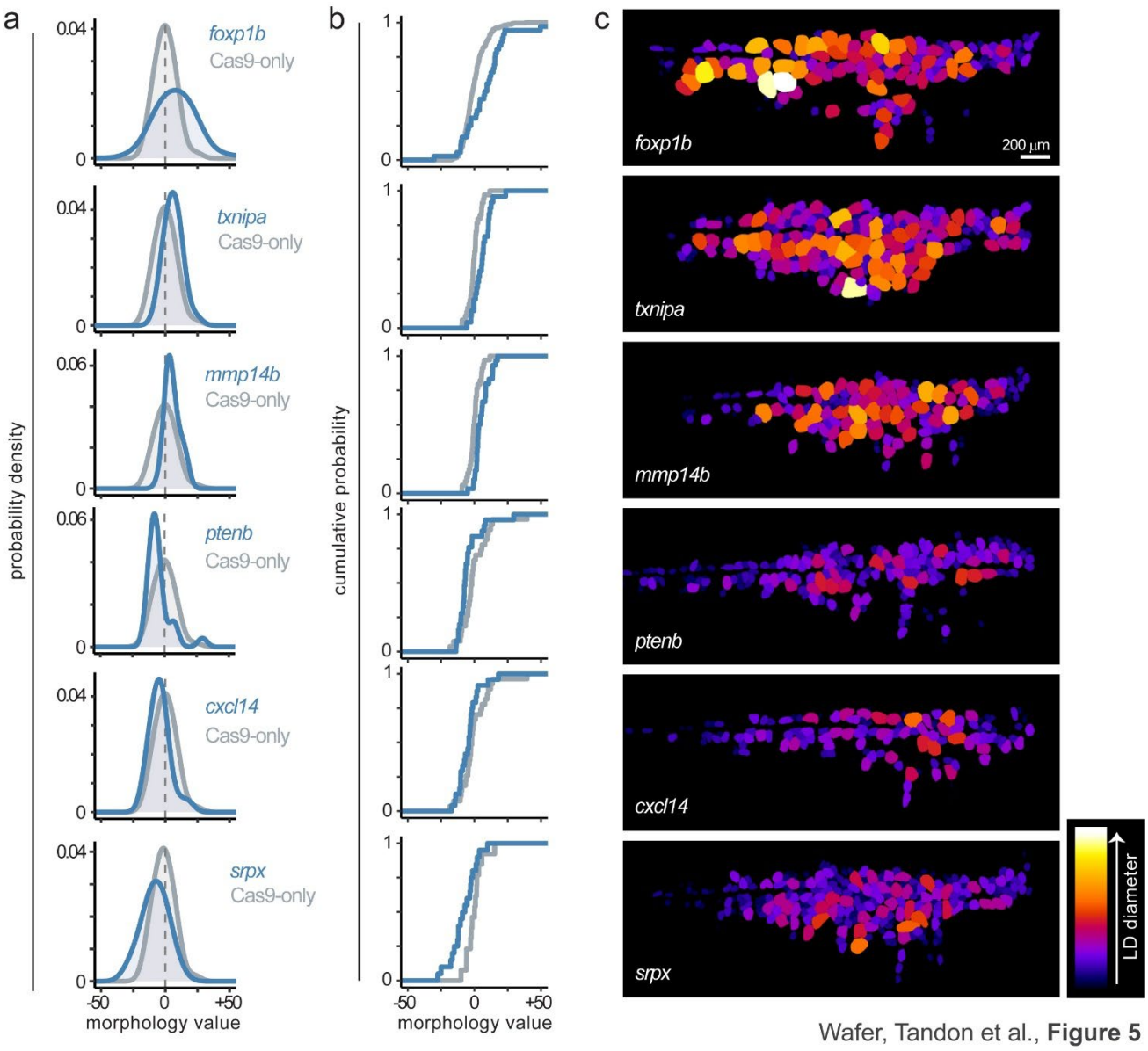

Figure 5. Identification of mutants with hypertrophic or hyperplastic adipose morphology. A. Morphology values for individual mutants (blue) with respect to their Cas-9 only control (grey). Dotted vertical line represents a morphology value of zero. **B.** Cumulative probability functions showing shift towards hypertrophic (*foxp1b*, *txnipa* and *mmp14b*) or hyperplastic (*ptenb*, *cxcl14* and *srpx*) morphology. **C.** Segmented subcutaneous adipose LDs from each respective mutant colour-coded according to LD diameter.

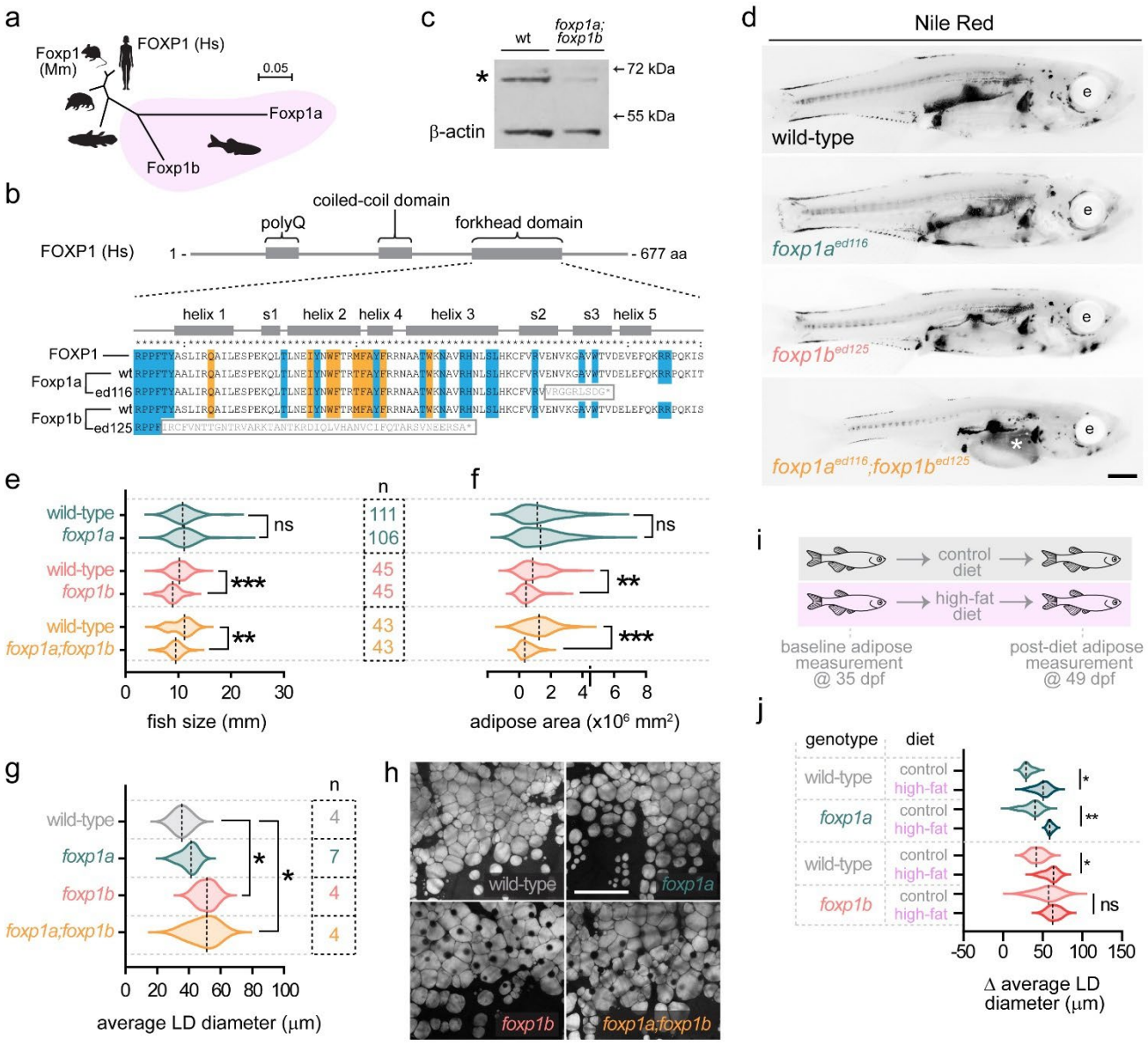

Wafer, Tandon et al., **Figure 6**

Figure 6. Stable *foxp1b* zebrafish mutants have hypertrophic adipose but are unable to undergo hypertrophic expansion in response to a high-fat diet. A. Phylogenetic tree showing relatedness of zebrafish Foxp1a and Foxp1b amino acid sequences to human, mouse, opossum and ceolocanth Focp1. Bar indicates substitutions per X. **B.** Overview of human Foxp1 domain structure showing a polyQ, coiled-coil and forkhead domain. Zoomed view of the DNA-binding forkhead domain showing structural features including helix and S. Essential amino acids of DNA binding are highlighted in orange, amino acids essential for DNA binding are highlighted in blue. Zebrafish wild-type Foxp1a and Foxp1b sequences are shown aligned to human, along with the ed116 foxp1a and ed125 foxp1b mutant alleles. Grey boxes show the addition of nonsense peptide followed by premature stop codon. **C.** Western blot showing the reduction of Foxp1 protein in double *foxp1a;foxp1b* zebrafish mutants. B-actin is used as a loading control. Asterisk indicates the Foxp1 protein band. **D.** Nile Red fluorescence images showing adipose lipid distribution (black signal) in wild-type, *foxp1a*^{ed116}, *foxp1b*^{ed125} and double *foxp1a*^{ed116}*;foxp1b*^{ed125} zebrafish mutants. E indicates the eye. Asterisk indicates lipid accumulation within the liver in double mutants. Scale bar is 1 mm. **E.** Violin plots

782 showing fish size (standard length, mm) of foxp1a^{ed116}, foxp1b^{ed125} and double foxp1a^{ed116};foxp1b^{ed125}
783 mutants compared to wild-type siblings. **F.** Violin plots showing Nile Red-positive adipose area in
784 foxp1a^{ed116}, foxp1b^{ed125} and double foxp1a^{ed116};foxp1b^{ed125} mutants compared to wild-type siblings.
785 **G.** Violin plots showing average LD diameter in *foxp1a^{ed116}*, *foxp1b^{ed125}* and double
786 *foxp1a^{ed116};foxp1b^{ed125}* mutants compared to wild-type siblings. **H.** LipidTox stained LDs within
787 subcutaneous adipose of *foxp1a^{ed116}*, *foxp1b^{ed125}*, double *foxp1a^{ed116};foxp1b^{ed125}* mutants and wild-
788 type sibling. **I.** Overview of high-fat diet feeding experiment where zebrafish were genotyped and
789 Nile Red imaged at 35 dpf, before undergoing a 14-day high-fat diet immersion (5% chicken egg yolk)
790 for two hours daily in addition to normal feeding regimen. Control diet was two hour immersion in
791 system water daily. Post-diet Nile Red imaging was performed at 49 dpf. **J.** Violin plots showing effects
792 of diet and genotype on average LD diameter. Statistical tests were one-way ANOVA followed by a
793 Tukey's HSD post-hoc test.